A simple model to assess the impact of gravity waves on ice crystal populations in the Tropical Tropopause Layer

Milena Corcos[1], Albert Hertzog[1], Riwal Plougonven[2], and Aurélien Podglajen[3]

[1]Laboratoire de Météorologie Dynamique/IPSL, Sorbonne Université, Paris, France
[2]Laboratoire de Météorologie Dynamique/IPSL, Ecole Polytechnique, Institut Polytechnique de Paris, Palaiseau, France
[3]Laboratoire de Météorologie Dynamique/IPSL, CNRS, Ecole Polytechnique, Institut Polytechnique de Paris, Palaiseau, France

Correspondence: Milena Corcos (milena.corcos@lmd.ipsl.fr)

Abstract. The role of gravity waves on microphysics of tropical cirrus clouds and air parcel dehydration was studied using the combination of Lagrangian observations of temperature fluctuations and a 1.5 dimension model. High frequency measurements during isopycnal balloon flights were used to resolve the gravity wave signals with periods ranging from a few days to 15min. The detailed microphysical simulations with homogeneous freezing, sedimentation and a crude horizontal mixing represent the

5   slow ascent of air parcels in the Tropical Tropopause Layer. A reference simulation describes the slow ascent of air parcels in the tropical tropopause layer, with nucleation occurring only below the cold point tropopause with a small ice crystals density. The inclusion of the gravity waves modifies drastically the low ice concentration vertical profile and weak dehydration found during the ascent alone, with the increased ice crystal number and size distribution agreeing better with observations. Numerous events of nucleation occur below and above the cold point tropopause, efficiently restoring the relative humidity over ice to

10   equilibrium with respect to the background temperature, as well as increase the cloud fraction in the vicinity of the cold-point tropopause. The corresponding decrease in water vapor is estimated at 2 ppmv around the cold point tropopause.

1 Introduction

Cirrus clouds are frequent and stand out as an important component in the Earth climate system (Winker and Trepte, 1998; McFarquhar et al., 2000). In the Tropical Tropopause Layer (TTL), they notably regulate the amount of water vapor that enters

15   the stratosphere via the freeze-drying mechanism, i.e. ice particles forming near the cold point and sedimenting out of the ascending air masses (Jensen et al., 1996; Holton and Gettelman, 2001; Gettelman et al., 2002; Fueglistaler et al., 2009; Randel and Jensen, 2013). Stratospheric water vapor affects the Earth's radiative budget (Solomon et al., 2010), but also ozone destruction, surface climate and polar stratospheric clouds (Solomon et al., 1986; Toon et al., 1989). Microphysical characteristics of TTL cirrus, like ice crystal number density, size, and shape, have a strong influence on their radiative properties (Smith et al.,

20   1998). The size of ice crystals furthermore determines their sedimentation velocity, and therefore impacts TTL cirrus lifetimes as well as the upper-troposhere and stratospheric humidity (Jensen et al., 2001).

Cirrus clouds can form in-situ within the TTL (Pfister et al., 2001). The relative importance of homogeneous and heterogeneous freezing in the TTL is still debated Jensen et al. (2018). In-situ measurements found ice nuclei from anthropogenic

emissions such as soot, sulfate Chen et al. (1998) as well as a significant fraction of organic compounds Cziczo et al. (2004).
25 Jensen et al. (2001) argued that in mixtures of particles with different freezing thresholds, effective ice nuclei, even in a very
small amount can control the freezing and growth dynamics, but the competition for water vapor is relevant mainly during
slow updrafts when homogeneous nucleation only freezes small ice densities, comparable to the number of efficient ice nuclei
Kärcher and Lohmann (2002). Furthermore, measurements of RH_i ranging from 1.1 to 1.7 in this region Krämer et al. (2009)
seem to suggest that the majority of aerosols are hard to freeze; and the small amount of effective ice nuclei wouldn't fully
30 suppress homogeneous freezing. Thus, homogeneous freezing is expected to be prevalent in the TTL Kärcher (2004); Krämer
et al. (2009); Spichtinger and Krämer (2013).

Homogeneous freezing of aqueous aerosols is strongly sensitive to cooling rates (Jensen and Toon, 1994; Kärcher and
Lohmann, 2002), so that TTL cirrus life cycle and microphysical properties are sensitive to temperature perturbations induced
by gravity waves (Jensen and Pfister, 2004). Several idealized model studies explored the effects of wave-induced temperature
35 variability on cirrus properties (Kärcher, 2003; Jensen and Pfister, 2004; W. Haag, 2004; Hoyle et al., 2005). The associated
impact on dehydration in the TTL is still only partially understood though, as it notably depends on the amplitude and intrinsic
frequency of the wave driven perturbations (Pfister et al., 2001; Jensen and Pfister, 2004; Kim and Alexander, 2015; Schoeberl
et al., 2015), as well as on whether TTL cirrus form in-situ or are anvils of convective clouds (Kärcher et al., 2006; Corti et al.,
2008; Schiller et al., 2009; Spichtinger and Krämer, 2013; Schoeberl et al., 2014). A number of processes, with a wide range
40 of scales, affect the formation and evolution of cirrus clouds. Thus any modeling effort will induce important simplifications
or even ommisions on parts of the processes involved.

Detailed microphysical simulations of TTL cirrus have naturally used Lagrangian box models (Hoyle et al., 2005), which are
able to resolve the size distribution of ice crystals. Such models can notably estimate ice concentration maxima, yet a critical
45 limitation is their difficulty to infer the dehydration of air parcels and the evolution of cirrus clouds on timescales significantly
longer than that associated with nucleation. Other models track the size and heights of ice crystals in a curtain approach (Jensen
and Pfister, 2004). At larger scales, the Community Aerosol and Radiation Model for Atmospheres (CARMA) model (Toon
et al., 1988; Bardeen et al., 2008), which represents crystal formation, growth, aggregation and sedimentation, can be combined
with global circulation models. Ultimately though, detailed information about the temperature variability experienced by air
50 parcels is crucial to address the issue of small-scale dynamics impacts on cirrus clouds (Jensen et al., 2016). In that regard, su-
perpressure balloon observations providing in-situ measurements of wave driven temperature variability in a quasi-Lagrangian
framework were also used in idealized box-model simulations (Dinh et al., 2016; Jensen et al., 2016). These studies were
nevertheless limited by the absence of sedimentation, which has a prominent role in determining ice concentration in cirrus
clouds (Jensen et al., 2012, 2013b; Murphy, 2014).

55 This paper further addresses the question of gravity-wave impacts on in-situ tropical cirrus clouds. Our approach is to
combine Lagrangian observations of temperature fluctuations to a simplified representation of microphysics to assess both
TTL cirrus ice-crystal densities and dehydration efficiency. Our observation dataset is that collected during 8 superpressure
balloon flights in the deep tropics, realized in the frame of the first Stratéole-2 campaign. This campaign took place in the

2019 boreal winter, and the balloon flights recorded timeseries of temperature fluctuations at ~ 19 km of altitude for 3 months
60   typically. Our microphysical model is able to resolve ice crystal homegeneous nucleation and growth, as well as sedimentation.
It also includes a simplified representation of horizontal mixing, which has been found important in the life cycle and evolution
of long-lived TTL cirrus clouds (Dinh et al., 2010).

The plan of the article is as follows: the first Section provides details on our method and simulations. In the second Section,
TTL cirrus found in simulations with and without gravity waves are described. The following Section discusses in more details
65   the impacts of gravity waves on cirrus microphysical properties and dehydration efficiency. Our simulations are also compared
to in-situ observations of TTL cirrus clouds. Main conclusions are provided in the last Section.

2   Method

2.1   Balloon-derived Lagrangian temperature timeseries

The wave-resolving temperature timeseries used in this study are derived from superpressure balloons measurements collected
70   during the 2019 Strateole-2 campaign. During this campaign, eight balloons were launched by the "Centre National d'Etudes
Spatiales" (CNES) in November and December, from Mahé Island (55,52°E, 4.67°S) in the Indian Ocean. The balloons drifted
for two to three months at altitudes between ~ 18.5 km and ~ 20.5 km of altitude within the whole tropical belt. More
information about the balloon trajectories and their environment during the flights can be found in Corcos et al. (2021).

Superpressure balloons directly record the instrinsic periods of wave motions, i.e. the period of disturbances felt by air
75   parcels advected by the atmospheric flow (Nastrom, 1980; Hertzog and Vial, 2001). During the Strateole-2 campaign, each
balloon was carrying a TSEN instrument that records pressure and temperature every 30 s, hence resolving the whole gravity-
wave spectrum. In this study, we have chosen not to use the direct temperature measurements recorded onboard the balloons,
since they tend to be influenced by the flight chain wake during day. Instead, we have reconstructed temperature disturbances
from pressure measurements. This reconstruction is based on three assumptions: (i) wave perturbations are hydrostatic, which
80   enables us to relate the pressure disturbance to the balloon vertical displacement (ζ'_b), (ii) superpressure balloons drift on
constant-density surfaces (Vincent and Hertzog, 2014), and (iii) wave perturbations are fast enough so that they can be con-
sidered as adiabatic transformations. These assumptions are valid for waves with intrinsic periods significantly longer than the
Brunt-Väisälä period (~ 5 minutes in the lower stratosphere), but shorter than the radiative damping time in the TTL ($20 - 30$
days Gettelman et al., 2004).

85   The isentropic air parcel displacements (ζ') then relate to those of the balloons according to (e.g., Boccara et al., 2008;
Podglajen et al., 2016):

$$\zeta' = \frac{1}{\alpha} \zeta'_b \tag{1}$$

where

$$\alpha = \frac{g/c_p + \partial\overline{T}/\partial z}{g/R_a + \partial\overline{T}/\partial z} \tag{2}$$

with g is the gravitational acceleration, c_p and R_a the specific heat at constant pressure and perfect gas constant per unit mass for dry air respectively, and $\partial\overline{T}/\partial z$ the vertical gradient of the background temperature, estimated from ERA5. Then, following adiabaticity, the Lagrangian temperature fluctuations may be deduced (e.g., Podglajen et al., 2016):

$$T' = -\frac{g}{c_p}\zeta' \tag{3}$$

and are checked to be very close to the temperature measurements. To be consistent with the above assumptions and to specifically study the role of gravity waves in cirrus cloud microphysics, we have applied a Bessel band-pass filter to the balloon timeseries, with cutoff periods at 15 min and 1 day. We have checked that our results are qualitatively not sensitive to the filtering method.

It should be noted that the balloon data from Corcos et al. (2021) were obtained at altitudes slightly above that of interest (the upper TTL, 17 km). Contrary to Schoeberl et al. (2018), we did not reduce the amplitude of the stratospheric balloon fluctuations, since Lagrangian temperature fluctuations are expected to be roughly constant over that altitude range, contrary to Eulerian ones (Podglajen et al., 2016; Kärcher and Podglajen, 2019).

2.2 Microphysics model and experiment setup

2.2.1 1.5 dimensional representation of microphysics

Our microphysical model aims at studying the in-situ formation and evolution of cirrus clouds at high altitude. It is based on the model developed in Dinh and Durran (2012) and Dinh et al. (2016), which simulates the homogeneous nucleation and growth of ice crystals in a single box under varying temperature and pressure conditions. The evolution of ice crystals number and mass is detailed in 36 bins of size, with radius ranging from 0.25 μm to 0.1 mm. Nucleation occurs by freezing on aerosol described by one bin of size, since previous studies have shown that ice formation generated by homogeneous freezing is not very sensitive to the aerosol size distribution (Jensen and Toon, 1994). The aerosol concentration is chosen as $230/cm^3$, guided by observations of aerosols in the upper troposphere (Hermann et al., 2003). The nucleation rate is computed according to the formulae of Koop et al. (2000), which assume that the nucleation rate coefficients solely depend on the difference of activity between the liquid aerosol solution and ice. Nucleation therefore occurs for relative humidity with respect to ice (RHi) of 157-158%.

Dinh's box model did not allow a description of sedimentation. The size distribution makes it possible to estimate a terminal velocity for each size bin, and hence with an assumption on the box thickness an outgoing mass flux rate. In this zero dimension model however no ice can sediment into the box, so sedimentation effects are at best half described. We therefore extended the box model into a vertical dimension. A one dimensional model (Jensen et al., 2013a, 2016; Kärcher, 2002) has the disadvantage

of artificially constraining all fluid parcels to remain vertically aligned, we thus add a crude representation of vertical wind shear to also allow horizontal mixing of ice crystals. Thus, our representation is of 1.5 dimensions. The geometrical setup of
120 air parcels is displayed in Figure 1 (left panel).

The sedimentation fall speed is calculated assuming spherical shaped crystals, and is based on the Reynolds number (Re) of the flow around the crystals (Böhm, 1989, eq. 11). It uses an Oseen-Best regime for $0.01 < \mathrm{Re} < 300$, and a Stokes-Cunningham regime at smaller Re (Kärcher, 2003). The fraction of ice crystal number that sediments from one air parcel to that directly below ($f_s(r)$) is inferred assuming an uniform distribution of crystals in air parcels. It comes:

125 $$f_s(r) = w(r)\,dt/h \tag{4}$$

with r the radius of the ice crystal, h the thickness of the airmass, and dt the time step of the model. The vertical shear of horizontal wind (s) furthermore contributes to advecting horizontally ice crystals during their sedimentation. Our implementation of sedimenting ice crystals includes a module aimed at a rough representation of wind shear (figure 1 right panel). Namely, during a time δt, a given row of air parcels (at a given altitude) has moved to that immediately above or below by $sh\,\delta t$. When
130 this displacement becomes larger than half of the air parcel length (L), we randomly shuffle the air parcels. This thus happens every $l/(2sh)$. Unless otherwise noted, we assume a vertical shear typical of the tropical UTLS: $s = 10$ m/s/km.

The nucleation and growth of ice crystals simulated by our model is validated by comparison to Spichtinger and Krämer (2013). We find the same relationship between constant vertical updraught speeds and ice crystals number concentration: a power-law variation for the slower vertical speeds and a saturation in ice crystal number associated with the pre-existing
135 background aerosol reservoir for the highest speeds (Spichtinger and Gierens (2009)). The simulated amount of ice crystals is furthermore found to be of the same order of magnitude.

2.2.2 Model dynamics

The temperature evolution of individual air parcels in the model includes two different processes. First, diabatic heating forces air parcels to slowly ascend through the TTL (Fueglistaler et al., 2009). This mean vertical motion is represented in the model
140 by a constant vertical speed $\bar{w} = 0.5$ mm/s, typical of the TTL (e.g., Jensen et al., 2001; Boehm and Lee, 2003; Salby and Callaghan, 2004). As air parcels ascend diabatically, their temperature adjusts on a background temperature profile ($\overline{T}$, see Figure 2) representative of the TTL (Kärcher and Podglajen, 2019). Second, air parcels optionally undergo adiabatic temperature disturbances generated by gravity waves. To represent these fluctuations, a time sample with the same duration than that of simulation is randomly chosen in the balloon-borne temperature-disturbance timeseries for each model air parcel indepen-
145 dently. While these wave-driven Lagrangian temperature disturbances are associated with air-parcel vertical displacements in the real atmosphere, we do not track those vertical motions in the model. Doing this, we assume that the wave-driven disturbances are associated with linear waves, inducing on average zero net vertical displacement. The altitudes of air parcels in the model therefore only evolve due to the slow diabatic ascent.
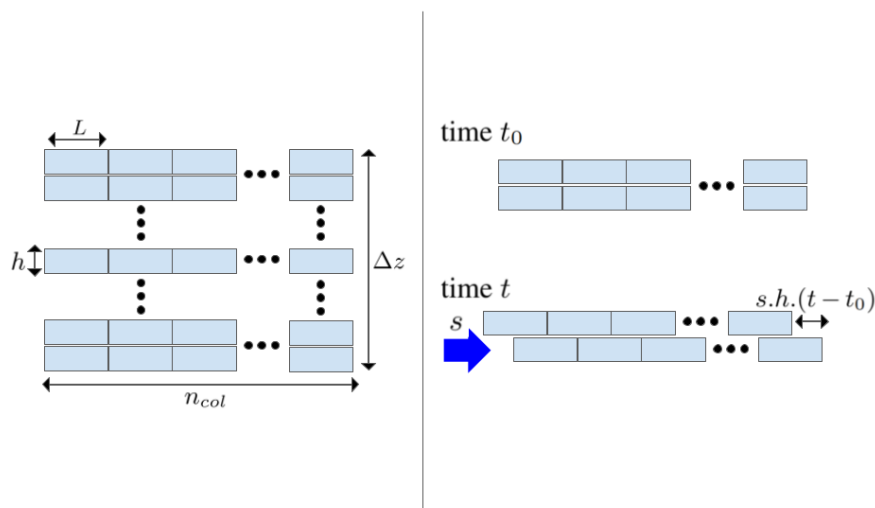
Figure 1. (Left) Representation of the modelled air parcels distributed among columns. (Right) Representation of the wind shear impact on two consecutive layers of air parcels. All letters are listed in table 1.

Two obvious limitations of the model need to be highlighted: first, we did not attempt to represent the correlation of wave-
150 driven temperature fluctuations between nearby air parcels. In a sense, our simulations thus maximize the random effect of gravity waves in microphysical processes. Second, our microphysical model does not represent the dynamics induced by the cloud itself, such as turbulence or radiatively-driven effects. Our simulations therefore apply to situations where those effect can be neglected at first order, i.e. optically thin cirrus associated with weak heating rates (Jensen et al., 2016).

2.2.3 Model configurations

155 The simulation geometry (number of rows and columns) and that of individual air parcels (vertical thickness and horizontal length) are free parameters of the model. In the simulations displayed in this study yet, we have always used the same geometry: 6 columns of 70 rows with 15-m thick, 150-m long air parcels. In particular, the air-parcel thickness was set as in Jensen et al. (2010), i.e. allowing the growth of ice crystals within the air parcel while maintaining a fine vertical resolution. Sensitivity tests have shown that our results do not depend on this specific choice.

160 Four simulations are performed in this study to assess the impact of gravity waves on ice crystals populations. First, a no-wave control simulation (NW) aims at representing TTL cirrus clouds generated by the slow radiative ascent only. The three other simulations all include wave-induced temperature perturbations. A preliminary simulation (wave first test, "WFT") starts with the same (large) initial relative humidity (RHi_0) than the no-wave simulation. We argue in the following that this is not the optimal choice for a wave simulation. Hence, we will discuss in more details the third simulation (W), in which $RHi_0 = 1$.
165 Last, in the no-mixing experiment ("NM"), we toggle off the mixing module in order to test the sensitivity of our results to this effect. The input parameters of all simulations are summarized in Table 1.

| Parameters | Symbol | No Wave | Waves (first test) | Waves | Waves (no mixing) |
		NW	"WFT"	W	"WNM"
Number of air parcels	n	420	420	420	420
Number of columns	n_{col}	6	6	6	6
Thickness of air parcels	h	15 m	15 m	15 m	15 m
Length of air parcels	L	150 m	150 m	150 m	150 m
Altitude span of setup	$\Delta z = h \frac{n}{ncol}$	1050 m	1050 m	1050 m	1050 m
Mean vertical speed	$\bar{w}$	0.5 mm/s	0.5 mm/s	0.5 mm/s	0.5 mm/s
Standard deviation of wave-induced temperature perturbations	$\sigma(T')$	0	1.5 K	1.5 K	1.5 K
Wind shear	s	10 m/s/km	10 m/s/km	10 m/s/km	0
Duration of simulation	Δt	72.2 h	h	51.5 h	37 h
Initial RHi	RHi_0	1.5	1.57	1	1

Table 1. Table of simulation definitions

The relative humidity at the start of the simulation (RHi_0) is constant along the whole column. RHi_0 varies between our simulations and the choice of this parameter is further discussed below, but we will see that longer simulations remove the sensitivity to the initial relative humidity.

3 Results

3.1 The slow-ascent simulation

The NW simulation corresponds to a 72-h ascent of air parcels encompassing the cold-point tropopause. During that time frame, air parcels have ascended for ~ 130 m. Due to the slow vertical speed, the associated cooling rates are very low, typically ± 4 mK/h (Figure 2). The initial relative humidity ($RHi_0 = 1.57$) is chosen close enough to the nucleation threshold, so that nucleation occurs during the simulation. We will first qualitatively describe the ice formation, its evolution in time and altitude, and then focus on the population of ice crystals.

Figure 3 displays the evolution of the ice mass and ice crystal number as a function of time and altitude for the lower-altitude air parcels only. Indeed, the three main nucleation events that occurred during the simulation were all located below the cold point, as the air parcels above will only warm up in time.

These nucleation events start first in the lowest layers of the setup. This can be understood since these layers are those where the temperature gradient is the most negative (see Fig 2). Hence, air parcels located in the lower part of the setup experience the largest cooling rates, and nucleate first. Below an initial altitude of ~ 17.1 km, all air parcels undergo at least one nucleation event, which occurs later and later as altitude increases (and the absolute temperature gradient decreases). In contrast, the RHi of air parcels located closer (or even above) the cold point never crosses the nucleation threshold.
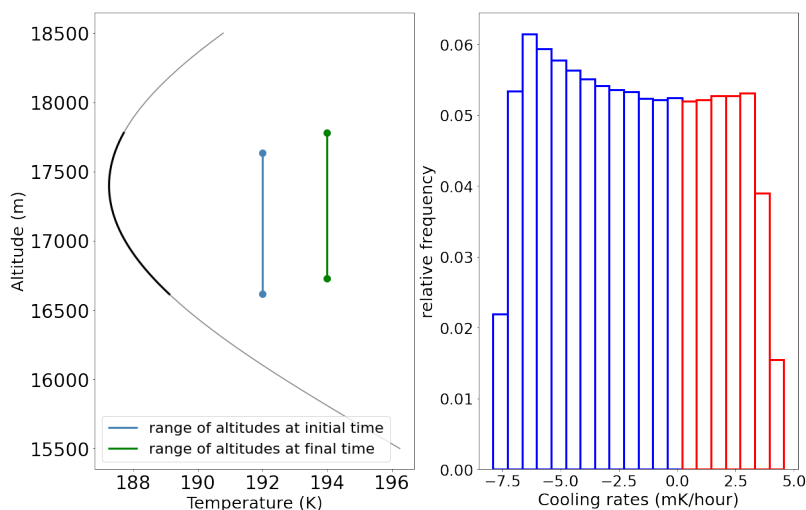
Figure 2. (Left) Temperature profile based on Kärcher and Podglajen (2019) radiosonde measurements in the tropics (171° E, 7° N), averaged over a year. The range of temperatures seen by air parcels in the NW simulation is highlighted in black. The initial and final altitude ranges of air parcels are indicated by the blue and green vertical bars respectively. (Right) Corresponding cooling rates with an ascent speed of 0.5 mm/s.

185   This dependence of the cooling rates with altitude also explains that the largest numbers of nucleated ice crystals are found in the lowest layers of the simulated domain (e.g., Spichtinger and Krämer, 2013). The second and third nucleation events produce less ice crystal number and less ice mass, partly because they occur higher up and are thus associated with lower cooling rates and partly because air masses have already been depleted in water vapor by ice crystals that have sedimented out before. Last, growth and sedimentation of the crystals account for the time shift of a few hours between the maximum of ice

190 crystals number and the maximum of ice mass, which is especially observed during the first two nucleation events.

    The evolution in time and altitude of the crystal size distribution during the NW simulation is displayed in Figure 4. The time evolution (left panel) and altitude evolution (right panel) are respectively a vertical average and a time average over the whole domain. The time evolution clearly exhibits the three nucleation events: at $t < 10$ h, $t \sim 20 - 30$ h, and $t \sim 40$ h. During those, ice crystals reach $5\ \mu$m within less than 1 h, while it takes ~ 5 h for them to grow beyond $15\ \mu$m. This timescale, which

195 is associated with the very low temperatures of the tropical tropopause, is prone to include modulation of the crystal growth by gravity waves, as suggested in Dinh et al. (2016) and Podglajen et al. (2018). Beyond $15\ \mu$m, the ice crystals tend to sediment quickly out of the model domain, so that the size distribution in this NW simulation is fairly narrow and peaks at $\sim 14\ \mu$m, in agreement with previous results (e.g. Jensen et al., 2010).

    This is further illustrated in Figure 5, which shows typical timescales for sedimentation and growth of ice crystals depending

200 on their size. Regarding sedimentation, the timescale shown corresponds to the time needed for half of the ice crystals to leave an air parcel of height $h = 15$ m. The timescale associated with crystal growth depends on supersaturation ($\mathrm{RH_i} - 1$), and is
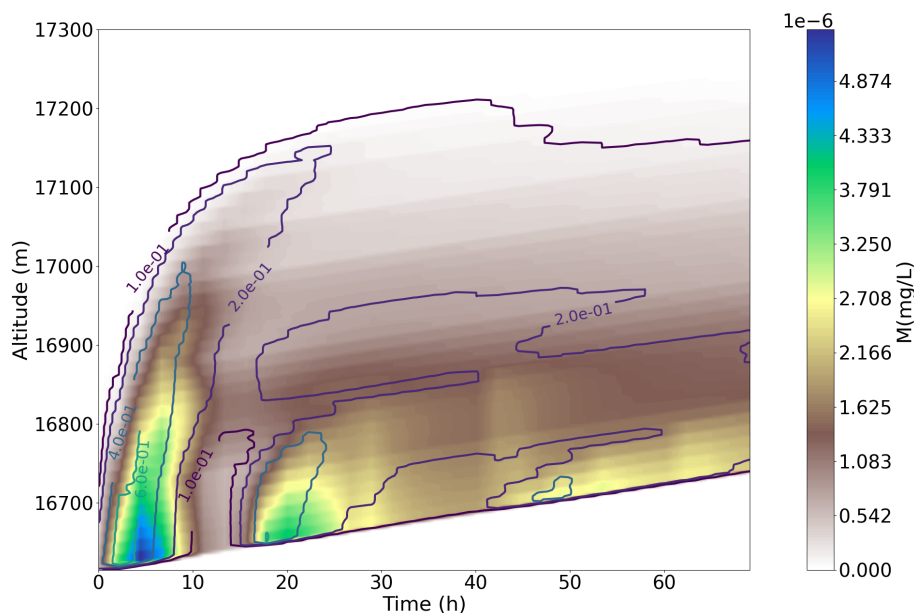
Figure 3. Evolution of ice mass (in $mg\,L^{-1}$, color) and ice crystal number (in L^{-1}, contours) in time and altitude for a simple slow ascent of 420 air parcels. Note that the altitude range is restricted to the lower part of the simulation domain.

displayed for a supersaturation typical of the NW simulation (0.6) as well as for a lower value (0.25), which will be used later on. In the NW simulation, the two timescales are of similar value for ice particles with $r = 7\,\mu m$. Indeed, it can be observed on the right panel of Figure 4 that particles with larger radii are not observed in the upper layers where nucleation occurs.

205 Hence, particles with $r > 7\,\mu m$ typically grow while they sediment, and are thus not encountered in the layers where they have nucleated. The sedimentation timescale for the bulk of the largest particles ($r \sim 15\,\mu m$) in the NW simulation is $1/10$ hr. Since those particles are observed 5 hr after the start of the simulation, they have typically fallen over $50\,h = 450$ m, which corresponds to the height difference between the model base and the uppermost layer where nucleation occurs (Fig. 4). On the other hand, the sedimentation timescale for ice crystals with $r < 3 - 4\,\mu m$ is one order of magnitude larger than their growth

210 timescale, and those particles are then mostly observed in the layer where they have nucleated.

3.2 The gravity-wave simulations

3.2.1 A preliminary experiment

A first test simulation that includes wave-induced temperature perturbations ("WFT") is performed with an initial relative humidity close to the nucleation threshold ($RHi_0 = 1.57$), as in the NW simulation. The evolution of the mean relative humidity

215 in the simulated domain is displayed in Figure 6. The wave-driven temperature perturbations trigger multiple events of nucleation, and the stronger cooling rates encountered by air parcels hugely increase the ice crystal production in comparison with the NW simulation, as already highlighted in previous studies (Dinh et al., 2016; Jensen et al., 2016; Kärcher et al., 2019).
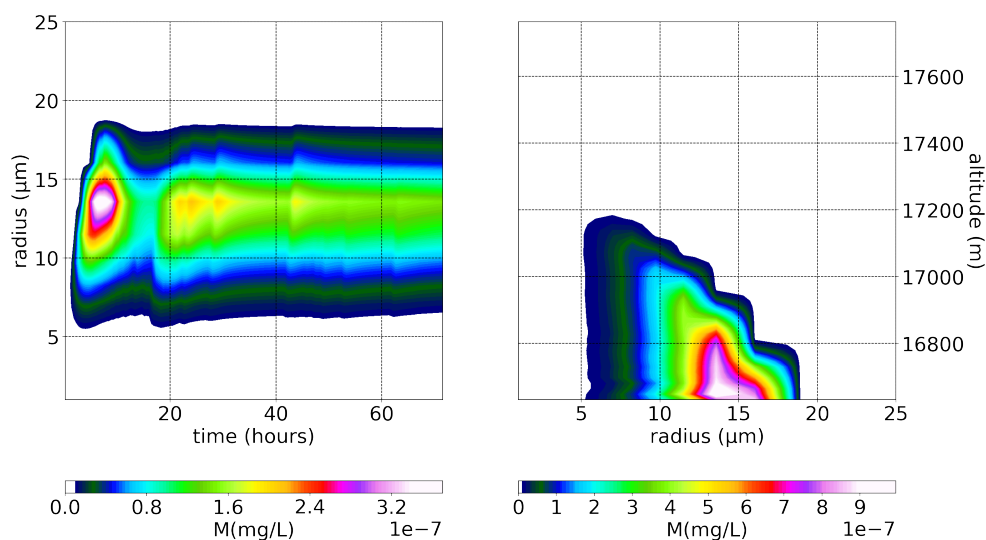
Figure 4. Evolution of ice mass in time (left) and altitude (right) for the NW simulation. Bins filled with more than one ice crystal per cubic meter are colored.

The ice crystal growth in the supersaturated environment efficiently depletes the water vapor, and the mean relative humidity consequently decreases within a few hours toward a value close to equilibrium (0.95). This behavior is in stark contrast with the

220 NW simulation, where the low number of ice crystals produced did not succeed to significantly reduce the relative humidity. It is a strong indication that waves likely allow a faster dehydration of air parcels more efficient, than the slow large-scale ascent.

Yet, the initial decrease in relative humidity seen in the "WFT" simulation is unlikely to occur in the real atmosphere and rather indicates a flaw in the initial relative humidity which is inconsistent with the ubiquitous presence of gravity waves. We therefore designed a more realistic wave experiment (W) that starts with an initial relative humidity of 1, and is described in

225 more details in the following section. During this simulation, the domain-averaged RHi varies in a very limited range.

3.2.2 A more realistic wave simulation

As already mentioned, one major effect of gravity waves is to widen the distribution of heating/cooling rates experienced by air parcels. This is illustrated in Figure 7, which shows the temperature timeseries for two air parcels respectively located below and above the cold point tropopause, as well as the probability distribution function of heating/cooling rates in the whole

230 domain. Recall that the temperature fluctuations are random samples of balloon observations in the tropical lower stratosphere. The short-period wave-driven perturbations obviously dominate the either negative or positive temperature trend associated
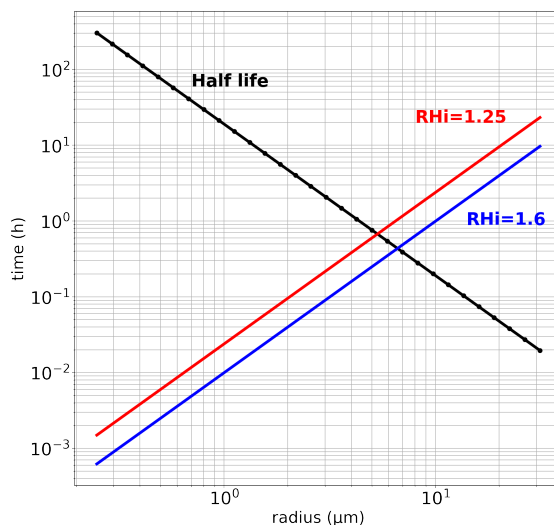
Figure 5. Half time (black), growth rate for RHi=1.25 (red) and RHi=1.6 (blue) depending on ice crystals size.
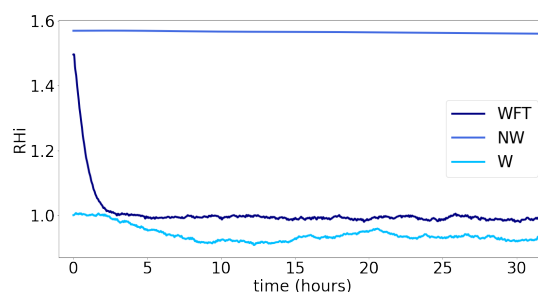
Figure 6. Evolution of relative humidity with respect to ice for the simulations "WFT", NW and W.

with the large-scale ascent. The standard deviation of heating/cooling rates in the wave simulations is 5 K/h, i.e. a thousand time larger than in the NW simulation, which drastically modifies ice production.

Figure 8 displays the evolution of the mean ice mass in the simulated domain in the W simulation. In contrast with the NW simulation, nucleation occurs almost constantly during the whole duration of the simulation. Furthermore, as the wave-induced temperature fluctuations are dominating air parcels temperature evolution, ice crystals are produced at all altitudes, even above the mean cold point tropopause (~ 17.4 km). Two distinct behaviors can be observed in the figure: first, some of the ice crystals are slowly advected upward at the same speed than air masses. They stay in the nucleating layer. This corresponds to small-size crystals, which typically need several tens of hours to sediment out of the air mass in which they have nucleated (cf. Figure 5). These crystals may eventually re-sublimate when air parcels experience a warm temperature
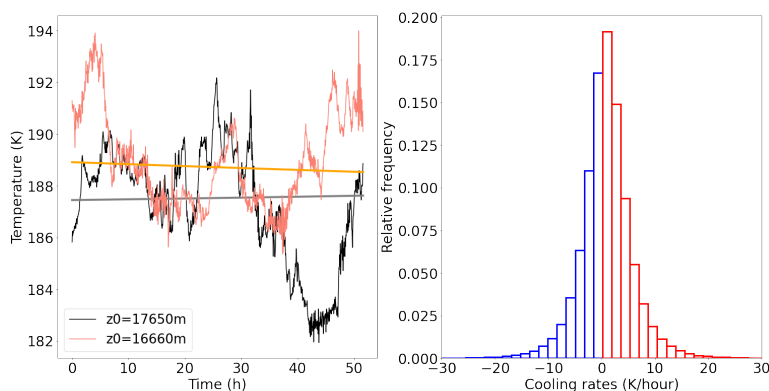
Figure 7. (Left) Timeseries of temperature for two air parcels at different altitudes. Background temperature interpolated from Kärcher and Podglajen (2019) radiosonde is superposed. (Right) Corresponding cooling rates with an ascent speed of 0.5 mm/s.

disturbance, and will therefore have little (if any) effect on the dehydration of air parcels. On the other hand, the largest ice crystals sediment out efficiently, widen the cloud layer and dilute the initial amount of ice. They contribute to dehydrate air parcels. Several fall streaks associated with sedimenting crystals are observed in Figure 8. Some fall speeds are superimposed on the figure to illustrate that those larger crystals have typical sizes between 3 and 8.5 μm. Note that the fall streaks are

245 well fitted assuming ice crystals with constant radii, in an environment close to equilibrium (RHi ≈ 1). Larger crystals may be created by a comparatively small temperature perturbation, a quenched nucleation (Dinh et al., 2016), or even ice crystals that have nucleated in response to a previous temperature fluctuation and which damp the wave-driven evolution of RHi (Jensen et al., 2010; Spichtinger and Krämer, 2013). This stresses that bigger crystals can be found at all altitudes and not only at the lower levels after sedimentation.

250 Overall, the ice mass field in this W simulation is much more heterogeneous than in the NW simulation. This heterogeneity certainly results from the uncorrelated timeseries of wave-induced temperature disturbances between air parcels, even though Figure 8 shows the mean ice mass field and therefore somewhat damps out a part of the inter-parcel differences. Yet, we note that this heterogeneity is also reminiscent of high resolution profiles of cloud properties, like those obtained during the ATTREX experiment (Jensen et al., 2013a).

255 Figure 9 displays the evolution in time and altitude of the crystal-size distribution during the W simulation. The time evolution exhibits some striking differences with the corresponding figure for the NW simulation. First, ice crystals hardly grow larger than 8μm when wave effects are included, i.e. half the maximum size reached in the NW simulation. The ice mass is mostly associated with ice-crystal radii of $3 - 6 \mu$m, i.e. a factor 3 to 4 smaller than in the NW simulation. The typical growth timescale of the largest crystals (~ 10 h) is also much slower. This can be first understood since the larger cooling rates induced

260 by wave perturbations contribute to nucleate a larger number of ice crystals than when only the slow ascent is responsible for nucleation. These numerous ice crystals then deplete water vapor more efficiently from the gas phase, and therefore grow more
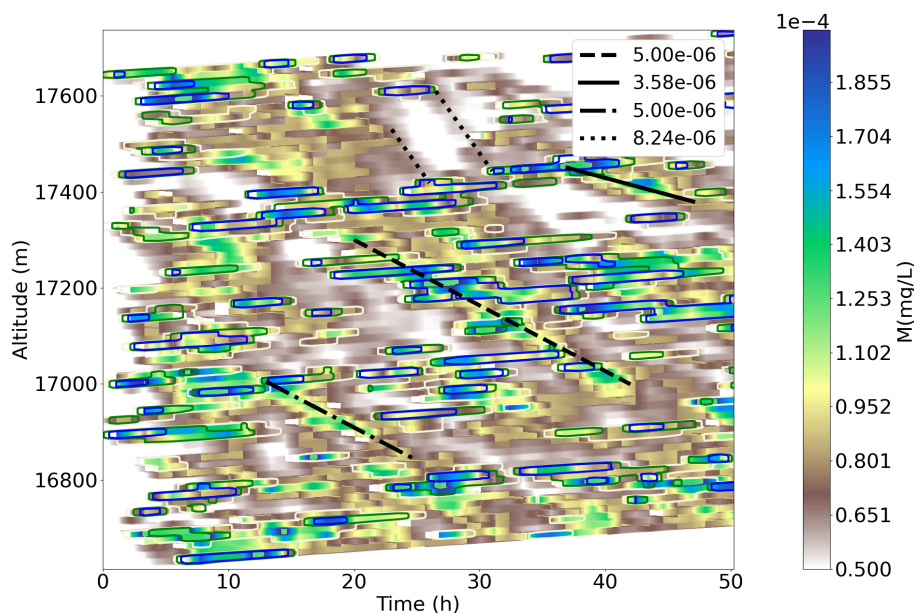
Figure 8. Evolution of ice mass in time and altitude for W simulation. Contours are representing the number of ice crystals /L, light brown N=1000, green N=2500, blue N=5000

slowly than in the NW simulation. This first effect is illustrated in Figure 5, which shows in red the characteristic growth time of ice crystals at a lower supersaturation (0.25) than that of the NW simulation (0.6). The 0.25 supersaturation value corresponds to one standard deviation of supersaturation in the W simulation. The ice crystal growth times are twice as large at this overall

265 lower supersaturation than in the W simulation, but still remain somewhat shorter than those inferred from Figure 9. A second wave effect that furthermore contributes to slowing the ice crystal growth timescale is the encounter of warm temperature disturbances by air parcels. Indeed, ice crystals larger than $\sim 5\,\mu$m have typical growth timescale larger than 1 hr, allowing wave-induced temperature fluctuations to potentially reduce the supersaturation over that timescale.

The altitude evolution once again illustrates the distinct behavior of small ice crystals with radius $r < 2 - 3\,\mu$m, which

270 tend to essentially remain and grow in the air mass in which they have nucleated, and that of larger ice crystals that tend to essentially sediment out of it. In the W simulation, the sedimentation is observed as soon as the crystals reach radii larger than $5\,\mu$m, in agreement with the lower overall supersaturation of this simulation (see Fig. 5). The altitude evolution also highlights the correlation between crystal sizes and their sensitivity to high-frequency temperature fluctuations: the larger the radius, the less the sensitivity. Smaller crystals respond quickly to their environment and are therefore easier to sublimate if a warm

275 wave-induced temperature fluctuation creates subsaturation.

Interestingly, ice crystals with radii larger than $5\,\mu$m are observed throughout the simulated domain in the W simulation, and even above the cold point tropopause. A possible nucleation mechanism for those high-altitude large crystals may be quenched nucleation events, as suggested in Dinh et al. (2016): as the background temperature increases in the stratosphere, waves will progressively create shorter and shorter nucleation events, which will limit the number of produced ice crystals and allow them
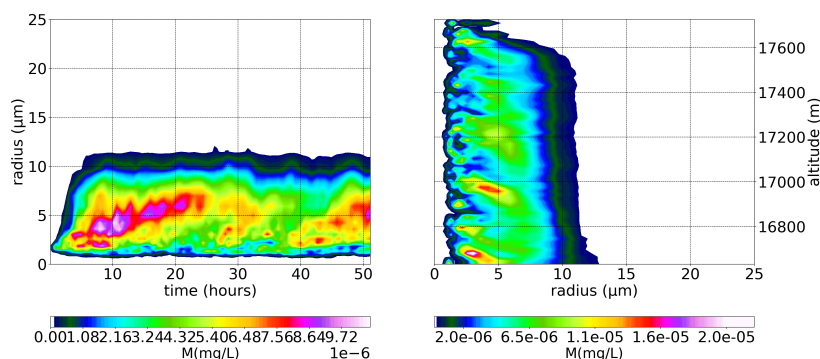
Figure 9. Evolution of ice mass in time (left) and altitude (right) for a simple slow ascent of 420 air parcels. Bins filled with more than 1 crystal per cubic meter are filled.

280 to grow more efficiently. Sedimentation hence occurs at all altitudes in the W simulation, which furthermore highlights that waves likely contribute to the dehydration of air parcels in the TTL.

4 Discussion

4.1 Ice production with and without waves and comparison with measurements

The main characteristics of ice production in the no-wave and wave simulations are summarized in Table 2. The most striking
285 feature is the difference of four orders of magnitude between the overall mean ice crystal concentrations (N_{ice}) in the simulations with and without gravity waves, which results from waves triggering more nucleation events and generating larger cooling rates than the mere slow ascent in the TTL. The condensed mass in the W simulation is decreased by a factor ~ 100 only with respect to that in the NW simulation, since ice crystals are of smaller sizes when wave perturbations are included. The overall cloud fraction, defined here as the fraction of time where $N_{ice} > 10\,\mathrm{L}^{-1}$ in at least one parcel per column, is null in the NW simulation
290 and almost 100% in the W simulation.

Figure 10 furthermore presents the ice-crystal size distributions in the W and NW simulations. As mentioned previously, the size distributions of ice crystals differ significantly when wave perturbations are included or not. The small cooling rates associated with the slow ascent enable ice crystals to efficiently grow until they sediment out of the air mass, leading to a relatively narrow size distribution centered around $r \sim 10\,\mu$m. On the other hand, both the competition between the numerous
295 ice crystals produced by large wave-induced cooling rates and the potential quenching of crystal nucleation or growth by wave-induced warm anomalies result in a wider size distribution and a smaller mean size ($r \sim 2\,\mu$m). The inclusion of horizontal mixing further reduces the size of ice crystals, but this is clearly a second-order effect in our simulations. This effect might nevertheless be more pronounced in a more realistic (less random) wave-perturbation field.

	Min size (μm)	Max size (μm)	Mean size (μm)	Mean concentration (/L)	Mean mass (μg)	Cloud fraction (%)
no wave (NW)	2.5	18	9.3	0.1	58	0
waves (W)	0.3	13	1.6	1385	0.5	98

Table 2. Characteristics of ice crystals produced in the simulations with or without gravity waves. The cloud fraction is defined as the fraction of time where $N_{ice} > 10\,L^{-1}$.
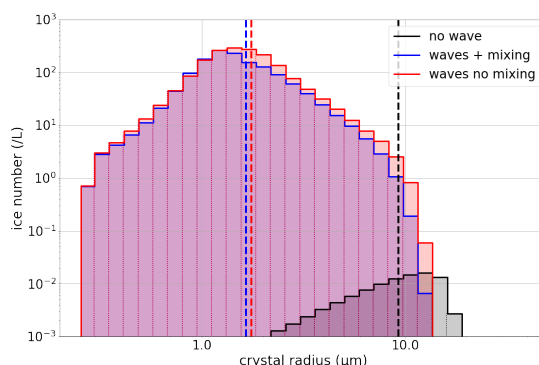
Figure 10. Ice-crystal size distributions in the (black) no-wave, (red) wave, and (blue) wave and mixing simulations. The mean size of each distribution is shown by vertical bars of the corresponding color.

Our simulations of ice-crystal population are now compared to observations of ice particles performed during the NASA
300 Airborne Tropical Tropopause EXperiment (ATTREX) campaign in 2014 (Jensen et al., 2013c, 2017). ATTREX collected high-resolution in-situ observations of cloud microphysics in the TTL during several flights of the Global Hawk unmanned aerial vehicle. The flights were performed out of Guam (13°N, 144°E), in the western Pacific, and lasted for $13-19$ hr at a maximum altitude of ~ 18 km. In this study, we will compare our simulation results with the tropical part of the transit flight from California to Guam on January 16th, as well as flights on February 12th, March 4th and 6th that sample various types of
305 TTL cirrus. On March 4th, the TTL was perturbed by the nearby presence of tropical cyclone Faxai, even though the Global Hawk did not sample the direct outflow of the cyclone (Jensen et al., 2017). In ATTREX flights, cloud properties were first measured with the Fast Cloud Droplet Probe (FCDP) spectrometer. The FCDP measures the forward scattered laser light from each cloud particle present in the sampling volume and deduces the size of the cloud particles from 1 to 50 μm diameter (Lance et al., 2010). We also compare our simulations with observations obtained by the 2D-S stereo probe (Lawson et al.,
310 2006) during the first flight of the ATTREX deployment. 2D-S measures particles with radii between 2.5 and 1,500 μm, but we have limited the comparison to the first two 2D-S bins, respectively associated with a mean radius of 5 and 10 μm. Only the 10 last hours of simulation are used for the comparisons, so as to avoid any effect of the initial conditions.

Ice-crystal concentrations in our simulations and in ATTREX observations are displayed in Figure 11. Note that the minimum detectable concentrations respectively are $\sim 10\,L^{-1}$ and $\sim 0.1\,L^{-1}$ for the FCDP and 2D-S instruments. In agreement with

315 previous findings (e.g., Schoeberl et al., 2015), the NW simulation produces unrealistically low crystal concentrations. On the other hand, ice-crystal concentrations obtained with the W simulation shows a fair agreement with observations. The main difference lies in the overestimation of ice-crystal concentrations larger than $1,000\,\mathrm{L}^{-1}$ in the simulation. These large concentrations are associated with fresh nucleation events for the largest cooling rates, which might not be easy to capture with observations. We nevertheless note that ice crystal numbers as large as $15,000\,\mathrm{L}^{-1}$ have been reported in ATTREX

320 observations (Jensen et al., 2013a). On the other hand, the similarity of the distributions for the lower concentrations ($\mathrm{N_{ice}} < 100\,\mathrm{L}^{-1}$), which are the most frequent, is relatively surprising. It has indeed been proposed that those low concentrations could result from heterogeneous nucleation on solid ice nuclei (e.g., Jensen et al., 2013a). Our simulations seem to indicate that homogeneous nucleation may also produce such low ice-crystal concentrations with reasonable probability of occurrence, in accordance with Spichtinger and Krämer (2013). Recent results (Baumgartner et al., 2022) have indicated that the density of

325 homogeneously nucleated ice crystals is sensitive to the size distribution of aerosols. Our simulations used a monodisperse aerosol distribution with $r_a = 250$ nm, consistent with observations performed during the balloon flights. Yet, the observed distributions are relatively broad, and therefore contain aerosols with larger sizes. Those large aerosol nucleate first, and reduce the available humidity for smaller aerosols. We nevertheless expect that this sensitivity of the nucleated ice-crystal number to the aerosol size should be rather small in our simulations, since the mean radius used is comparable to the observed one. If any,

330 it would contribute to reduce the number of nucleated ice crystals.

Figure 12 displays the comparisons of ice-crystal size distribution between our simulations and FCDP observations. The results associated with the simulation without wave-induced fluctuations are not shown here because of its low crystal concentrations. In agreement with the measurable concentrations by the FCDP instrument, we have only retained air parcels with $\mathrm{N_{ice}} > 10\,\mathrm{L}^{-1}$ in the W simulation for this comparison. We note that the comparison of ice crystal size distribution should be

335 taken cautiously as FCDP was designed for measurements of water droplets. The size retrieval actually assumes Mie scattering in spherical particles (Lance, 2012; Lance et al., 2010), and therefore bears uncertainties associated with the sizing of non-spherical ice crystals. Woods et al. (2018) nevertheless showed a tendency toward quasi-spheroid particles when particle sizes (and temperature) decrease. The simulated crystal sizes in the W simulation fall in the range of ATTREX observations, i.e. radii between 1 and 15 μm, and the distribution shapes are fairly consistent. The increased occurrence of smaller particles in

340 the simulation might be associated with limitations of the FCDP instrument at sizes near $1\,\mu$m. On the other hand, one possible reason for the lower occurrence of $\sim 10\mu$m particles in the W simulation is the limited altitude range of this simulation, which contribute to preclude the growth of sedimenting particles.

4.2 Air parcel dehydration

It is now commonly accepted that gravity waves likely play a role in dehydration processes in the TTL, and therefore in

345 setting the stratospheric water vapor content (e.g., Kim and Alexander, 2015; Schoeberl et al., 2015). The primary effect of gravity waves is to lower the temperature experienced by air parcels as they ascend through the TTL. Yet, dehydration only occurs when produced ice crystals are able to sediment out of the air parcel in which they have nucleated. At low temperatures characteristic of the tropical cold point tropopause, the typical timescales of crystal nucleation, growth and sedimentation are
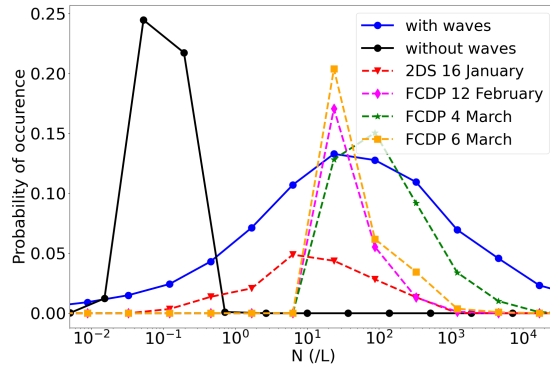
Figure 11. Comparison of ice crystal concentrations in (solid black) the NW and (solid blue) the W simulations, and (dashed) 2014 ATTREX measurements. In ATTREX measurements, the minimum detectable concentration by the FCDP and 2D-S instruments respectively are $\sim 10\,\mathrm{L}^{-1}$ and $0.1\,\mathrm{L}^{-1}$
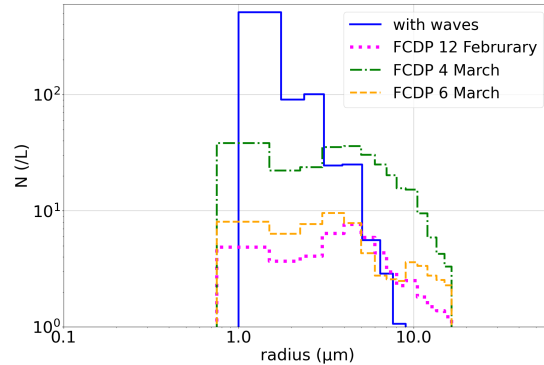
Figure 12. Comparison of ice crystal size distribution in the W simulation and in 2014 ATTREX FCDP measurements. Distributions are shown in cloud fraction only, i.e. $N_{\mathrm{ice}} > 10\,\mathrm{L}^{-1}$.

of the same order of magnitude as gravity-wave periods. Hence, TTL dehydration results from the complex coupling of wave-
350 induced temperature perturbations and microphysical processes, which for instance include nucleation or growth quenching (Spichtinger and Krämer, 2013; Dinh et al., 2016; Jensen et al., 2016; Schoeberl et al., 2015) and sedimentation-wave phasing (Podglajen et al., 2018). The dehydration efficiency is notably controlled by the crystal-size distribution, which critically depends on gravity-wave perturbations, as our simulations have shown.

Figure 13 displays the relative evolution of water vapor mixing ratio as a function of the final altitude of air parcels in the W
355 simulation, i.e.:

$$\delta_{\mathrm{H_2O}}^{\mathrm{rel}} = \frac{X_{\mathrm{H_2O}}^{\mathrm{final}} - X_{\mathrm{H_2O}}^{\mathrm{initial}}}{X_{\mathrm{H_2O}}^{\mathrm{initial}}} \times 100 \tag{5}$$
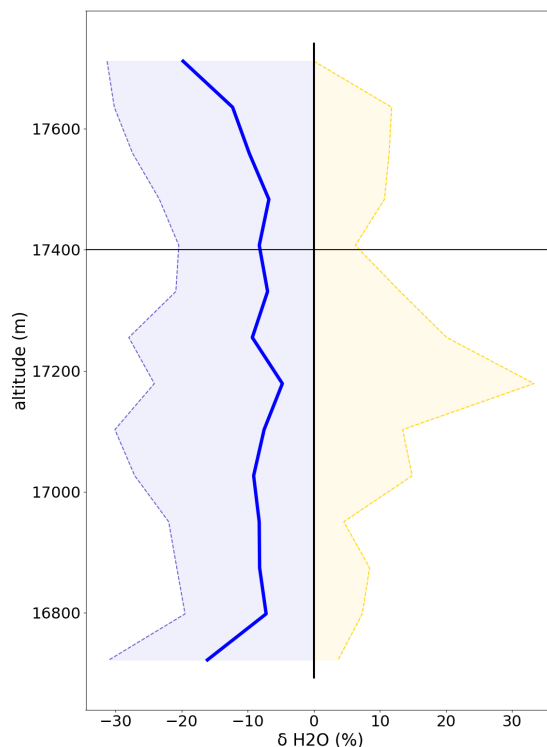
Figure 13. Relative dehydration ($\delta_{\mathrm{H_2O}}^{\mathrm{rel}}$) of air parcels in the W simulation: (thick) Mean dehydration, (thin) 25th and 75th quantiles. The altitudes shown correspond to the final altitudes of air parcels. The mean cold point is indicated by the thin horizontal line at 17.4 km. The relative dehydration in the NW simulation is hardly discernible from the 0% vertical line.

where $X_{\mathrm{H_2O}}$ stands for the water vapor mixing ratio. The mean net effect of gravity waves is to dehydrate air parcels by $\sim 5\%$ throughout the simulated altitudes, in agreement with Fig. 6. Yet, Figure 13 exhibits a large variability in dehydration at a given altitude, which results from different water vapor redistribution through nucleation and sedimentation in the different model
360 columns. In particular, air parcels can be rehydrated as ice crystals sedimenting from above sublimate in them (Dinh et al., 2010; Murphy, 2014). In the uppermost layers of the domain though, i.e. above the mean cold-point tropopause located at 17.4 km, dehydration becomes more systematic, and the net wave-induced dehydration is increased to $\sim 20\%$. This suggests that final wave-induced dehydration events may actually occur above the climatological cold point tropopause.

Table 3 shows the observed water vapor mixing ratios in both the NW and W simulations for those of the air parcels that are
365 above the mean cold-point tropopause at the end of the simulations, as well as mixing ratios associated with relative humidities over ice of 1 and 1.6 at the mean cold-point temperature. In the NW simulation, the mean cold-point temperature is that shown in Figure 2, i.e. $\overline{T}(17.4\,\mathrm{km})$. In the W simulation, the mean cold-point temperature is computed as the mean of the minimum

Simulation	$\overline{T_{\mathrm{CP}}}$ (K)	$X_{\mathrm{H_2O}}(\mathrm{RHi}=1)$ (ppmv)	$X_{\mathrm{H_2O}}(\mathrm{RHi}=1.6)$ (ppmv)	Stratospheric $X_{\mathrm{H_2O}}$ (ppmv)
NW	187.2	2.3	3.7	3.9
W	184.1	1.3	2.2	1.8

Table 3. Water vapor mixing ratios in the W and NW simulations. The stratospheric $X_{\mathrm{H_2O}}$ corresponds to the mean water vapor mixing ratio of those air parcels that are above the mean cold-point tropopause at the end of the simulation.

temperature experienced by each air parcel that has crossed 17.4 km (Kim and Alexander, 2015). First, no dehydration is observed in the NW simulation: the very small number of ice crystals created in this simulation were very inefficient in
370 depleting water vapor (see Fig. 6). In this run, the stratospheric water-vapor mixing ratio (3.9 ppmv) thus corresponds to that of the air parcels initially, which was set at RHi= 1.57 over the whole altitude range. Because of this initial constant relative humidity, the stratospheric mixing ratio is slightly higher than that at the cold point. One may note that none of the air parcels in which nucleation occurred have crossed the tropopause during the NW simulation, so that the real stratospheric mixing ratio would have been (very) slightly reduced in a longer run.

375 On the other hand when gravity waves are included, the stratospheric water-vapor mixing ratio is 1.8 ppmv . This value lies in between the extreme mixing ratios obtained with RHi=1 and RHi=1.6 at the cold point. Hence, as expected, gravity waves are not fully efficient in restoring RHi=1 at the minimum temperature experienced by the air parcels (Schoeberl et al., 2015). Yet, this water vapor mixing ratio is slightly lower than the mixing ratio corresponding to RHi=1 at the background temperature (2.3 ppmv), in agreement with the 20% increased dehydration observed in the uppermost layers of the W simulation (cf.
380 Fig. 6). When compared to the NW case, the stratospheric water vapor mixing ratio is thus decreased by ~ 2 ppmv when gravity-wave perturbations are included. The magnitude of this systematic wave-induced dehydration is very significant, since it is for instance comparable to the seasonal variation of water vapor at the tropical tropopause (e.g. Mote et al., 1996; Davis et al., 2016).

5 Conclusions

385 This study aimed at investigating the effects of gravity waves on the microphysics of cirrus clouds and air parcel dehydration at the tropical tropopause layer in idealized simulations. Detailed microphysical simulations, which consider homogeneous nucleation as the sole mechanism for ice production, sedimentation and a crude treatment of horizontal mixing, have been carried out with and without gravity-wave temperature perturbations. Excerpts from quasi-Lagrangian balloon-borne observations in the lower tropical stratosphere are used to add gravity-wave disturbances in otherwise slowly ascending air parcels in the TTL.
390 Two main simulations are carried out and contrasted to highlight the profoundly different outcomes in terms of microphysics, depending on the inclusion of gravity waves effects. A reference simulation represents the ascension of air parcels in the tropical tropopause layer, initially close to nucleating conditions ("NW" simulation), the second one also represents the impact of gravity wave-driven temperature variability in a non saturated environment ("W" simulation).

The "NW" simulation indicates that without wave perturbations, i.e. when only the slow ascent of air parcels in the TTL is
395   responsible for nucleation events, ice crystal concentrations are unrealistically low. Similarly, the ice-crystal size distribution
is too narrow, and peaks at a radius of 9 μm, which is too large when compared to observations. Lastly, the "NW" simulation
is associated with almost zero dehydration in the vicinity of the cold-point tropopause, despite initial conditions close to the
homogeneous nucleation threshold.

The inclusion of gravity waves significantly modifies the production of ice crystals in the simulation. This is notably due to
400   the much larger cooling/heating rates produced by gravity waves. The more numerous nucleation events in the wave simulation
contribute to efficiently restoring the relative humidity over ice to equilibrium with respect to the background temperature
profile throughout the simulated domain. A further 20% decrease in water vapor mixing ratio is observed in air parcels that
have penetrated in the stratosphere. The wave-induced dehydration effect is thus estimated to ~ 2 ppmv in the vicinity of the
cold-point tropopause.

405   Ice crystal number concentration and size distribution compare furthermore better with observations in the gravity-wave
simulation, even though no cloud condensation nuclei are included in the simulations. This supports that heterogeneous nucle-
ation might not be the only process responsible for lower ice crystals concentrations. Furthermore, this accordance highlights
the importance of a realistic representation of waves to reproduce observations.

Our results bring further evidence that gravity waves may significantly increase the cloud fraction in the vicinity of the
410   cold-point tropopause, as also suggested in, e.g., Ueyama et al. (2015) and Schoeberl et al. (2018). A precise assessment of
this increase would require less idealized simulations than those carried out here. Similarly, the radiative impact of the wave-
induced enhanced cloudiness is left for future work. Our results nonetheless call for a coupled treatment of TTL wave and
microphysics in parameterizations used in climate models.

Data availability. The balloon-born TSEN data is part of Strateole-2 and available at https://data.ipsl.fr/catalog/strateole2/.
415   Stratéole-2 is sponsored by CNES, CNRS/INSU, ESA and NSF. ATTREX data are available at
https://espoarchive.nasa.gov/archive/browse/attrex/id4/GHawk

Author contributions. The authors confirm contribution to the paper as follows:
Formal analysis and methodology : Milena Corcos, Albert Hertzog, Aurélien Podglajen and Riwal Plougouven
Draft manuscript preparation: Milena Corcos
420   Writing of the original draft : Milena Corcos and Albert Hertzog
All authors reviewed the results and approved the final version of the manuscript.

Competing interests. The authors declare that they have no conflict of interest.

Acknowledgements. The authors would like to thank warmly Eric Jensen and Bernd Kärcher for thoughful discussions and suggestions during the final stage of this study, as well as Martina Bramberger, Joan Alexander and Sean Davis.

References

Bardeen, C. G., Toon, O. B., Jensen, E. J., Marsh, D. R., and Harvey, V. L.: Numerical simulations of the three-dimensional distribution of meteoric dust in the mesosphere and upper stratosphere, J. Geophys. Res., 113, https://doi.org/10.1029/2007jd009515, 2008.

Baumgartner, M., Rolf, C., Grooß, J.-U., Schneider, J., Schorr, T., Möhler, O., Spichtinger, P., and Krämer, M.: New investigations on homogeneous ice nucleation: the effects of water activity and water saturation formulations, Atmos. Chem. Phys., 22, 65–91, https://doi.org/10.5194/acp-22-65-2022, 2022.

Boccara, G., Hertzog, A., Vincent, R. A., and Vial, F.: Estimation of Gravity Wave Momentum Flux and Phase Speeds from Quasi-Lagrangian Stratospheric Balloon Flights. Part I: Theory and Simulations, J. Atmos. Sci., 65, 3042–3055, https://doi.org/10.1175/2008JAS2709.1, 2008.

Boehm, M. T. and Lee, S.: The Implications of Tropical Rossby Waves for Tropical Tropopause Cirrus Formation and for the Equatorial Upwelling of the Brewer–Dobson Circulation, J. Atmos. Sci., 60, 247–261, https://doi.org/10.1175/1520-0469(2003)060<0247:tiotrw>2.0.co;2, 2003.

Böhm, H. P.: A General Equation for the Terminal Fall Speed of Solid Hydrometeors, J. Atmos. Sci., pp. 2419–2427, https://doi.org/10.1175/1520-0469(1989)046<2419:ageftt>2.0.co;2, 1989.

Chen, Y., Kreidenweis, S. M., McInnes, L. M., Rogers, D. C., and DeMott, P. J.: Single particle analyses of ice nucleating aerosols in the upper troposphere and lower stratosphere, Geophys. Res. Lett., 25, 1391–1394, https://doi.org/10.1029/97gl03261, 1998.

Corcos, M., Hertzog, A., Plougonven, R., and Podglajen, A.: Observation of Gravity Waves at the Tropical Tropopause Using Superpressure Balloons, J. Geophys. Res., 126, https://doi.org/10.1029/2021jd035165, 2021.

Corti, T., Luo, B. P., de Reus, M., Brunner, D., Cairo, F., Mahoney, M. J., Martucci, G., Matthey, R., Mitev, V., dos Santos, F. H., Schiller, C., Shur, G., Sitnikov, N. M., Spelten, N., Vössing, H. J., Borrmann, S., and Peter, T.: Unprecedented evidence for deep convection hydrating the tropical stratosphere, Geophys. Res. Lett., 35, https://doi.org/10.1029/2008gl033641, 2008.

Cziczo, D. J., DeMott, P. J., Brooks, S. D., Prenni, A. J., Thomson, D. S., Baumgardner, D., Wilson, J. C., Kreidenweis, S. M., and Murphy, D. M.: Observations of organic species and atmospheric ice formation, Geophys. Res. Lett., 31, https://doi.org/10.1029/2004gl019822, 2004.

Davis, S. M., Rosenlof, K. H., Hassler, B., Hurst, D. F., Read, W. G., Vömel, H., Selkirk, H., Fujiwara, M., and Damadeo, R.: The Stratospheric Water and Ozone Satellite Homogenized (SWOOSH) database: a long-term database for climate studies, 8, 461–490, https://doi.org/10.5194/essd-8-461-2016, 2016.

Dinh, T. and Durran, D. R.: A hybrid bin scheme to solve the condensation/evaporation equation using a cubic distribution function, Atmos. Chem. Phys., 12, 1003–1011, https://doi.org/10.5194/acp-12-1003-2012, 2012.

Dinh, T., Podglajen, A., Hertzog, A., Legras, B., and Plougonven, R.: Effect of gravity wave temperature fluctuations on homogeneous ice nucleation in the tropical tropopause layer., Atmos. Chem. Phys., 16, 35–46, https://doi.org/10.5194/acp-16-35-2016, 2016.

Dinh, T. P., Durran, D. R., and Ackerman, T. P.: Maintenance of tropical tropopause layer cirrus, J. Geophys. Res., 115, https://doi.org/10.1029/2009jd012735, 2010.

Fueglistaler, S., Dessler, A. E., Dunkerton, T. J., Folkins, I., Fu, Q., and Mote, P. W.: Tropical tropopause layer, Rev. Geophys., 47, https://doi.org/10.1029/2008RG000267, 2009.

Gettelman, A., Salby, M. L., and Sassi, F.: Distribution and influence of convection in the tropical tropopause region, J. Geophys. Res., 107, ACL 6–1–ACL 6–12, https://doi.org/10.1029/2001jd001048, 2002.

Gettelman, A., de F. Forster, P. M., Fujiwara, M., Fu, Q., Vömel, H., Gohar, L. K., Johanson, C., and Ammerman, M.: Radiation balance of the tropical tropopause layer, J. Geophys. Res., 109, https://doi.org/https://doi.org/10.1029/2003JD004190, 2004.

Hermann, M., Heintzenberg, J., Wiedensohler, A., Zahn, A., Heinrich, G., and Brenninkmeijer, C. A. M.: Meridional distributions of aerosol
465   particle number concentrations in the upper troposphere and lower stratosphere obtained by Civil Aircraft for Regular Investigation of the
       Atmosphere Based on an Instrument Container (CARIBIC) flights, J. Geophys. Res., 108, n/a–n/a, https://doi.org/10.1029/2001jd001077,
       2003.

Hertzog, A. and Vial, F.: A study of the dynamics of the equatorial lower stratosphere by use of ultra-long-duration balloons: 2. Gravity
       waves, J. Geophys. Res., 106, 22 745–22 761, https://doi.org/10.1029/2000JD000242, 2001.

470 Holton, J. R. and Gettelman, A.: Horizontal transport and the dehydration of the stratosphere, Geophys. Res. Lett., 28, 2799–2802,
       https://doi.org/10.1029/2001gl013148, 2001.

Hoyle, C. R., Luo, B. P., and Peter, T.: The Origin of High Ice Crystal Number Densities in Cirrus Clouds, J. Atmos. Sci., 62, 2568–2579,
       https://doi.org/10.1175/jas3487.1, 2005.

Jensen, E. J. and Pfister, L.: Transport and freeze-drying in the tropical tropopause layer, J. Geophys. Res., 109,
475   https://doi.org/10.1029/2003jd004022, 2004.

Jensen, E. J. and Toon, O. B.: Ice nucleation in the upper troposphere: Sensitivity to aerosol number density, temperature, and cooling rate,
       Geophys. Res. Lett., 21, 2019–2022, https://doi.org/10.1029/94gl01287, 1994.

Jensen, E. J., Toon, O. B., Pfister, L., and Selkirk, H. B.: Dehydration of the upper troposphere and lower stratosphere by subvisible cirrus
       clouds near the tropical tropopause, Geophys. Res. Lett., 23, 825–828, https://doi.org/10.1029/96gl00722, 1996.

480 Jensen, E. J., Pfister, L., Ackerman, A. S., Tabazadeh, A., and Toon, O. B.: A conceptual model of the dehydration of air due to
       freeze-drying by optically thin, laminar cirrus rising slowly across the tropical tropopause, J. Geophys. Res., 106, 17 237–17 252,
       https://doi.org/10.1029/2000jd900649, 2001.

Jensen, E. J., Pfister, L., Bui, T.-P., Lawson, P., and Baumgardner, D.: Ice nucleation and cloud microphysical properties in tropical tropopause
       layer cirrus, Atmos. Chem. Phys., 10, 1369–1384, https://doi.org/10.5194/acp-10-1369-2010, 2010.

485 Jensen, E. J., Pfister, L., and Bui, T. P.: Physical processes controlling ice concentrations in cold cirrus near the tropical tropopause, J.
       Geophys. Res., 117, https://doi.org/https://doi.org/10.1029/2011JD017319, 2012.

Jensen, E. J., Diskin, G., Lawson, R. P., Lance, S., Bui, T. P., Hlavka, D., McGill, M., Pfister, L., Toon, O. B., and Gao, R.: Ice nucleation
       and dehydration in the Tropical Tropopause Layer, Proc. National Academy of Sci., 110, 2041–2046, 2013a.

Jensen, E. J., Lawson, R. P., Bergman, J. W., Pfister, L., Bui, T. P., and Schmitt, C. G.: Physical processes controlling ice concentrations in
490   synoptically forced, midlatitude cirrus, J. Geophys. Res., 118, 5348–5360, https://doi.org/10.1002/jgrd.50421, 2013b.

Jensen, E. J., Pfister, L., Jordan, D. E., Fahey, D. W., Newman, P. A., Thornberry, T., Rollins, A., Diskin, G., Bui, T. P., McGill, M., et al.:
       The NASA Airborne Tropical TRopopause EXperiment (ATTREX), SPARC Newsletter, 41, 15–24, 2013c.

Jensen, E. J., Ueyama, R., Pfister, L., Bui, T. V., Alexander, M. J., Podglajen, A., Hertzog, A., Woods, S., Lawson, R. P., Kim, J.-E., and
       Schoeberl, M. R.: High-frequency gravity waves and homogeneous ice nucleation in tropical tropopause layer cirrus, Geophys. Res. Lett.,
495   43, 6629–6635, https://doi.org/10.1002/2016GL069426, 2016.

Jensen, E. J., Pfister, L., Jordan, D. E., Bui, T. V., Ueyama, R., Singh, H. B., Thornberry, T. D., Rollins, A. W., Gao, R.-S., Fahey, D. W.,
       Rosenlof, K. H., Elkins, J. W., Diskin, G. S., DiGangi, J. P., Lawson, R. P., Woods, S., Atlas, E. L., Rodriguez, M. A. N., Wofsy, S. C.,
       Pittman, J., Bardeen, C. G., Toon, O. B., Kindel, B. C., Newman, P. A., McGill, M. J., Hlavka, D. L., Lait, L. R., Schoeberl, M. R.,
       Bergman, J. W., Selkirk, H. B., Alexander, M. J., Kim, J.-E., Lim, B. H., Stutz, J., and Pfeilsticker, K.: The NASA Airborne Tropical

500 Tropopause Experiment: High-Altitude Aircraft Measurements in the Tropical Western Pacific, Bull. Am. Meteorol. Soc., 98, 129–143, https://doi.org/10.1175/BAMS-D-14-00263.1, 2017.

Jensen, E. J., Kärcher, B., Ueyama, R., Pfister, L., Bui, T. V., Diskin, G. S., DiGangi, J. P., Woods, S., Lawson, R. P., Froyd, K. D., and Murphy, D. M.: Heterogeneous Ice Nucleation in the Tropical Tropopause Layer, J. Geophys. Res., 123, https://doi.org/10.1029/2018jd028949, 2018.

505 Kim, J.-E. and Alexander, M. J.: Direct impacts of waves on tropical cold point tropopause temperature, Geophys. Res. Lett., 42, 1584–1592, https://doi.org/https://doi.org/10.1002/2014GL062737, 2015.

Koop, T., Luo, B., Tsias, A., and Peter, T.: Water activity as the determinant for homogeneous ice nucleation in aqueous solutions, Nature, 406, 611–614, https://doi.org/10.1038/35020537, 2000.

Krämer, M., Schiller, C., Afchine, A., Bauer, R., Gensch, I., Mangold, A., Schlicht, S., Spelten, N., Sitnikov, N., Borrmann, S., de Reus, M.,
510 and Spichtinger, P.: Ice supersaturations and cirrus cloud crystal numbers, Atmos. Chem. Phys., 9, 3505–3522, https://doi.org/10.5194/acp-9-3505-2009, 2009.

Kärcher, B.: Properties of subvisible cirrus clouds formed by homogeneous freezing, Atmos. Chem. Phys., 2, 161–170, https://doi.org/10.5194/acp-2-161-2002, 2002.

Kärcher, B.: Simulating gas-aerosol-cirrus interactions: Process-oriented microphysical model and applications, Atmos. Chem. Phys., pp.
515 1645–1664, https://doi.org/10.5194/acp-3-1645-2003, 2003.

Kärcher, B.: Cirrus clouds in the tropical tropopause layer: Role of heterogeneous ice nuclei, Geophys. Res. Lett., 31, n/a–n/a, https://doi.org/10.1029/2004gl019774, 2004.

Kärcher, B. and Lohmann, U.: A parameterization of cirrus cloud formation: Homogeneous freezing of supercooled aerosols, J. Geophys. Res., 107, AAC 4–1–AAC 4–10, https://doi.org/10.1029/2001JD000470, 2002.

520 Kärcher, B. and Podglajen, A.: A Stochastic Representation of Temperature Fluctuations Induced by Mesoscale Gravity Waves, J. Geophys. Res., 124, 11 506–11 529, https://doi.org/10.1029/2019jd030680, 2019.

Kärcher, B., Hendricks, J., and Lohmann, U.: Physically based parameterization of cirrus cloud formation for use in global atmospheric models, J. Geophys. Res., 111, https://doi.org/10.1029/2005jd006219, 2006.

Kärcher, B., Jensen, E. J., and Lohmann, U.: The Impact of Mesoscale Gravity Waves on Homogeneous Ice Nucleation in Cirrus Clouds,
525 Geophys. Res. Lett., 46, 5556–5565, https://doi.org/10.1029/2019GL082437, 2019.

Lance, S.: Coincidence Errors in a Cloud Droplet Probe (CDP) and a Cloud and Aerosol Spectrometer (CAS), and the Improved Performance of a Modified CDP, J. Atmos. Oceanic Technol., 29, 1532–1541, https://doi.org/10.1175/jtech-d-11-00208.1, 2012.

Lance, S., Brock, C. A., Rogers, D., and Gordon, J. A.: Water droplet calibration of the Cloud Droplet Probe (CDP) and in-flight performance in liquid, ice and mixed-phase clouds during ARCPAC, Atmos. Meas. Tech., 3, 1683–1706, https://doi.org/10.5194/amt-3-1683-2010,
530 2010.

Lawson, R. P., O'Connor, D., Zmarzly, P., Weaver, K., Baker, B., Mo, Q., and Jonsson, H.: The 2D-S (Stereo) Probe: Design and Preliminary Tests of a New Airborne, High-Speed, High-Resolution Particle Imaging Probe, J. Atmos. Oceanic Technol., 23, 1462–1477, https://doi.org/10.1175/JTECH1927.1, 2006.

McFarquhar, G. M., Heymsfield, A. J., Spinhirne, J., and Hart, B.: Thin and Subvisual Tropopause Tropical Cirrus: Observations and Radia-
535 tive Impacts, J. Atmos. Sci., 57, 1841–1853, https://doi.org/10.1175/1520-0469(2000)057<1841:tasttc>2.0.co;2, 2000.

Mote, P. W., Rosenlof, K. H., McIntyre, M. E., Carr, S. E., Gille, J. C., Holton, J. R., Kinnersley, J. S., Pumphrey, H. C., Russell III, J. M., and Waters, J. W.: An atmospheric tape recorder: The imprint of tropical tropopause temperatures on stratospheric water vapor, J. Geophys. Res., 101, 3989–4006, https://doi.org/https://doi.org/10.1029/95JD03422, 1996.

Murphy, D. M.: Rare temperature histories and cirrus ice number density in a parcel and a one-dimensional model, Atmos. Chem. Phys., 14, 13 013–13 022, https://doi.org/10.5194/acp-14-13013-2014, 2014.

Nastrom, G. D.: The Response of Superpressure Balloons to Gravity Waves, J. Applied Meteo., pp. 1013–1019, https://doi.org/10.1175/1520-0450(1980)019<1013:trosbt>2.0.co;2, 1980.

Pfister, L., Selkirk, H. B., Jensen, E. J., Schoeberl, M. R., Toon, O. B., Browell, E. V., Grant, W. B., Gary, B., Mahoney, M. J., Bui, T. V., and Hintsa, E.: Aircraft observations of thin cirrus clouds near the tropical tropopause, J. Geophys. Res., 106, 9765–9786, https://doi.org/10.1029/2000jd900648, 2001.

Podglajen, A., Hertzog, A., Plougonven, R., and Legras, B.: Lagrangian temperature and vertical velocity fluctuations due to gravity waves in the lower stratosphere, Geophys. Res. Lett., 43, 3543–3553, https://doi.org/10.1002/2016GL068148, 2016.

Podglajen, A., Plougonven, R., Hertzog, A., and Jensen, E.: Impact of gravity waves on the motion and distribution of atmospheric ice particles, Atmos. Chem. Phys., pp. 10 799–10 823, https://doi.org/10.5194/acp-18-10799-2018, 2018.

Randel, W. J. and Jensen, E. J.: Physical processes in the tropical tropopause layer and their roles in a changing climate, Nature Geoscience, 6, 169–176, https://doi.org/10.1038/ngeo1733, 2013.

Salby, M. and Callaghan, P.: Control of the Tropical Tropopause and Vertical Transport across It, J. Climate, 17, 965–985, https://doi.org/10.1175/1520-0442(2004)017<0965:cottta>2.0.co;2, 2004.

Schiller, C., Grooß, J.-U., Konopka, P., Plöger, F., dos Santos, F. H. S., and Spelten, N.: Hydration and dehydration at the tropical tropopause, Atmos. Chem. Phys., 9, 9647–9660, https://doi.org/10.5194/acp-9-9647-2009, 2009.

Schoeberl, M. R., Dessler, A. E., Wang, T., Avery, M. A., and Jensen, E. J.: Cloud formation, convection, and stratospheric dehydration, Earth and Space Science, 1, 1–17, https://doi.org/10.1002/2014ea000014, 2014.

Schoeberl, M. R., Jensen, E. J., and Woods, S.: Gravity waves amplify upper tropospheric dehydration by clouds, Earth and Space Sci., 2, 485–500, https://doi.org/10.1002/2015ea000127, 2015.

Schoeberl, M. R., Jensen, E. J., Pfister, L., Ueyama, R., Avery, M., and Dessler, A. E.: Convective Hydration of the Upper Troposphere and Lower Stratosphere, Journal of Geophysical Research: Atmospheres, 123, 4583–4593, https://doi.org/https://doi.org/10.1029/2018JD028286, 2018.

Smith, W. L., Ackerman, S., Revercomb, H., Huang, H., DeSlover, D. H., Feltz, W., Gumley, L., and Collard, A.: Infrared spectral absorption of nearly invisible cirrus clouds, Geophys. Res. Lett., 25, 1137–1140, https://doi.org/10.1029/97gl03491, 1998.

Solomon, S., Garcia, R. R., Rowland, F. S., and Wuebbles, D. J.: On the depletion of Antarctic ozone, Nature, 321, 755–758, https://doi.org/10.1038/321755a0, 1986.

Solomon, S., Rosenlof, K. H., Portmann, R. W., Daniel, J. S., Davis, S. M., Sanford, T. J., and Plattner, G.-K.: Contributions of Stratospheric Water Vapor to Decadal Changes in the Rate of Global Warming, Science, 327, 1219–1223, https://doi.org/10.1126/science.1182488, 2010.

Spichtinger, P. and Gierens, K. M.: Modelling of cirrus clouds – Part 1b: Structuring cirrus clouds by dynamics, Atmos. Chem. Phys., 9, 707–719, https://doi.org/10.5194/acp-9-707-2009, 2009.

Spichtinger, P. and Krämer, M.: Tropical tropopause ice clouds: a dynamic approach to the mystery of low crystal numbers, Atmos. Chem. Phys., 13, 9801–9818, https://doi.org/10.5194/acp-13-9801-2013, 2013.

Toon, O. B., Turco, R. P., Westphal, D., Malone, R., and Liu, M.: A Multidimensional Model for Aerosols: Description of Computational
575   Analogs, J. Atmos. Sci., 45, 2123–2144, https://doi.org/10.1175/1520-0469(1988)045<2123:ammfad>2.0.co;2, 1988.

Toon, O. B., Turco, R. P., Jordan, J., Goodman, J., and Ferry, G.: Physical processes in polar stratospheric ice clouds, J. Geophys. Res., 94,
11 359, https://doi.org/10.1029/jd094id09p11359, 1989.

Ueyama, R., Jensen, E. J., Pfister, L., and Kim, J.-E.: Dynamical, convective, and microphysical control on wintertime distributions of water
vapor and clouds in the tropical tropopause layer, J. Geophys. Res., 120, https://doi.org/10.1002/2015jd023318, 2015.

580 Vincent, R. A. and Hertzog, A.: The response of superpressure balloons to gravity wave motions, Atmos. Meas. Tech., 7, 1043–1055,
https://doi.org/10.5194/amt-7-1043-2014, 2014.

W. Haag, B. K.: The impact of aerosols and gravity waves on cirrus clouds at midlatitudes, J. Geophys. Res., 109,
https://doi.org/10.1029/2004jd004579, 2004.

Winker, D. M. and Trepte, C. R.: Laminar cirrus observed near the tropical tropopause by LITE, Geophys. Res. Lett., 25, 3351–3354,
585   https://doi.org/10.1029/98gl01292, 1998.

Woods, S., Lawson, R. P., Jensen, E., Bui, T. P., Thornberry, T., Rollins, A., Pfister, L., and Avery, M.: Microphysical Properties of Tropical
Tropopause Layer Cirrus, J. Geophys. Res., 123, 6053–6069, https://doi.org/10.1029/2017jd028068, 2018.